



Comparison of static and dynamic characteristics of 1550 nm quantum dash and quantum well lasers

BEI SHI,^{1,*}  SERGIO PINNA,¹ WEI LUO,²  HONGWEI ZHAO,¹ SI ZHU,² SIMONE T. SURAN BRUNELLI,¹ KEI MAY LAU,²  AND JONATHAN KLAMKIN¹ 

¹*Electronic and Computer Engineering Department, University of California Santa Barbara, Santa Barbara, CA 93106, USA*

²*Department of Electronic and Computer Engineering, Hong Kong University of Science and Technology, Clear Water Bay, Kowloon, Hong Kong, China*

**beishi@ucsb.edu*

Abstract: Compared to quantum well (QW) lasers, lower dimensional quantum dot (QD) or quantum dash (QDash) devices demonstrate superior performances, owing to their quantized energy levels and increased carrier confinement. Here, we report the systematic comparison of static and dynamic properties of long wavelength (1550 nm) QDash and QW lasers. For the QDash lasers, a higher maximum operating temperature and lower temperature dependence was achieved for long cavities, although the threshold current densities were larger than the QW reference devices. The lasing characteristics for QDashes are significantly improved following the application of a high reflectance (HR) coating on the rear facets. The QDash lasers also exhibit three orders lower dark current, of 45 $\mu\text{A}/\text{cm}^2$ under -1 V reverse bias. Small signal modulation on the $4 \times 550 \mu\text{m}^2$ Fabry-Perot cavities yields a modulation efficiency of 0.48 GHz/ $\sqrt{\text{mA}}$ and a maximum 3-dB bandwidth of 7.4 GHz for QDashes, slightly larger than that for the QW devices. Meanwhile, a stronger damping effect was observed for the QDash lasers due to their lower differential gain.

© 2020 Optical Society of America under the terms of the [OSA Open Access Publishing Agreement](#)

1. Introduction

Semiconductor QDs have been proposed as the “holy grail” for photonic devices since the 1980s, and in particular, QD lasers have witnessed a boost in development in the past decades [1–9]. To date, 1.3 μm InAs/GaAs QD lasers have demonstrated low thresholds with high differential gains, and desirable temperature stabilities. It is challenging, however, to extend their emission wavelength to the telecom C-band or even longer wavelengths for applications including free space communications, LiDAR, RF photonics, and sensing. This is primarily ascribed to the large lattice mismatch between InAs and the (In)GaAs barrier, generating a high density of defects that limits optical efficiencies in the longer wavelength regime [10]. As a promising solution, growing InAs QD or QDash materials on InP substrates can realize broadband emission from less than 1.2 μm to 2 μm , due to a reduced lattice mismatch for the InAs/InP system [11]. Yet, under standard growth conditions, these dots usually tend to elongate into dashes because of the complex strain distribution on (001) InP substrates [12]. To grow QDs on (001) InP, special growth interruption techniques and InGaAsP or InAlGaAs buffers are usually required [13–15]. Another approach to form circular dots involves growing InAs on vicinal (001) InP or higher index (311)B InP substrates [16,17]. Still, the InAs/InP QDash structures have been predicted possessing unique advantages such as reduced height dispersion and less sensitivity to size fluctuations than QDs [11,18]. So far, they have been applied in manufacturing high gain and low noise distributed feedback (DFB) lasers, high performance mode-locked lasers (MLLs),

and semiconductor optical amplifiers (SOAs) [19,20]. Additionally, QDash and QD lasers are also of great interest for silicon photonics due to their lower sensitivity to defects when growing by direct heteroepitaxy [5,21,22].

Pioneering research has been carried out comparing InP-based QD, QDash, and QW lasers. Alghoraibi *et al.* characterized the dependence of threshold on laser cavity lengths between QDs on (311) B InP and QDashes grown on (001) InP substrates [23]. Although the QDs exhibit lower threshold current densities (J_{th}), the deduced internal quantum efficiency (IQE) is higher for QDashes ($\eta_i=54\%$) than for QD lasers (39%). The threshold temperature stability is improved for QDs, with a higher characteristic temperature (T_0). Reithmaier *et al.* comprehensively reviewed the QW and QDash gain elements in broad-area, DFB and distributed Bragg reflector (DBR) lasers [11]. Results have suggested a lower J_{th} for QDashes with longer cavities, and an inversely higher J_{th} in shorter devices due to their lower modal gain compared to QWs. With regard to the temperature stability, QDash lasers also exhibit less temperature dependence. Additionally, the relative intensity noise (RIN) value for a $4.7 \mu\text{m} \times 2.5 \text{mm}$ ridge waveguide (RWG) QDash laser is below -160 dB/Hz, 10-15 dB lower than the record QW laser. Zilkie *et al.* measured the gain recovery time for QD, QDash, and QW semiconductor optical amplifiers (SOAs), of ~ 80 ps, ~ 300 ps, and ~ 500 ps, respectively [24]. This finding suggests that QD is the most promising candidate for ultrafast signal processing. Recently, Sadeev *et al.* compared the dynamic properties of metalorganic chemical vapor deposition (MOCVD) grown C-band QD and QDash RWG lasers [25]. Small signal measurements reveal a lower damping for QDashes and a larger 3-dB bandwidth for QDs. Under large signal modulations, the error-free data rate for QD lasers is 22.5 Gbit/s, and 17.5 Gbit/s for QDash lasers.

In this work, we performed both static and dynamic comparisons between 1550 nm seven-layer InGaAsP-based QW laser and three-stack InAs/InAlGaAs QDash laser, grown on (001) InP substrates. Specifically, although the J_{th} values of QW lasers are averagely 40% lower than the QDashes, a higher operation temperature and an improved temperature stability were acquired for long cavity QDash lasers. The thermal impedance (Z_T) for $20 \times 500 \mu\text{m}^2$ QDash lasers is $7.3 \text{ }^\circ\text{C/W}$, a bit larger than the QW counterparts of $5.7 \text{ }^\circ\text{C/W}$. The dark current levels of QDash lasers are three orders lower than the QW devices, of $45 \mu\text{A/cm}^2$ under -1 V biasing. After facets coating with HR dielectrics, a more dramatic improvement was achieved on QDash lasers, yielding tripled maximum output powers, approximately half J_{th} , enlarged slope efficiencies and T_0 values. Small signal modulation reveals a stronger resonance suppression for the QDash lasers, along with a lower K-factor and a higher modulation efficiency. The measured maximum 3-dB bandwidth for the $3 \times 550 \mu\text{m}^2$ QDash laser is 7.4 GHz. These comparisons enlighten potential applications for QDash materials in high operating temperature and high speed lasers, as well as low dark current photodiodes.

2. Experiments

Figures 1(a) and 1(b) illustrate schematic epitaxial device structures for the seven-layer InGaAsP-based QW and three-stack InAs/InAlGaAs QDash lasers grown with a horizontal-reactor low-pressure Thomas-Swan and Aix-200/4 MOCVD system, respectively. The QDash active region is first optimized with three-layer 3.6 monolayer (ML) InAs/30 nm InAlGaAs spacer, in order to obtain the best optical quality. The standard QW laser structure comprising seven layers of 6.5 nm $\text{In}_{0.73}\text{Ga}_{0.27}\text{As}_{0.85}\text{P}_{0.15}$ wells and 8 nm $\text{In}_{0.73}\text{Ga}_{0.27}\text{As}_{0.52}\text{P}_{0.48}$ barriers [26], was subsequently grown as the reference. The difference between the two structures primarily exist in the materials and layer numbers of active regions. It should be mentioned that the doping levels for their n-InP claddings were somewhat different, with the amount of 7.5×10^{17} - $1 \times 10^{18}/\text{cm}^3$ for QW and $5.5 \times 10^{17}/\text{cm}^3$ for Qdash laser. The total thicknesses of active layers were kept the same (~ 100 nm) for both structures to ensure similar surface recombination on the sidewall of the active region and carrier injection conditions. The QDash surface morphology was

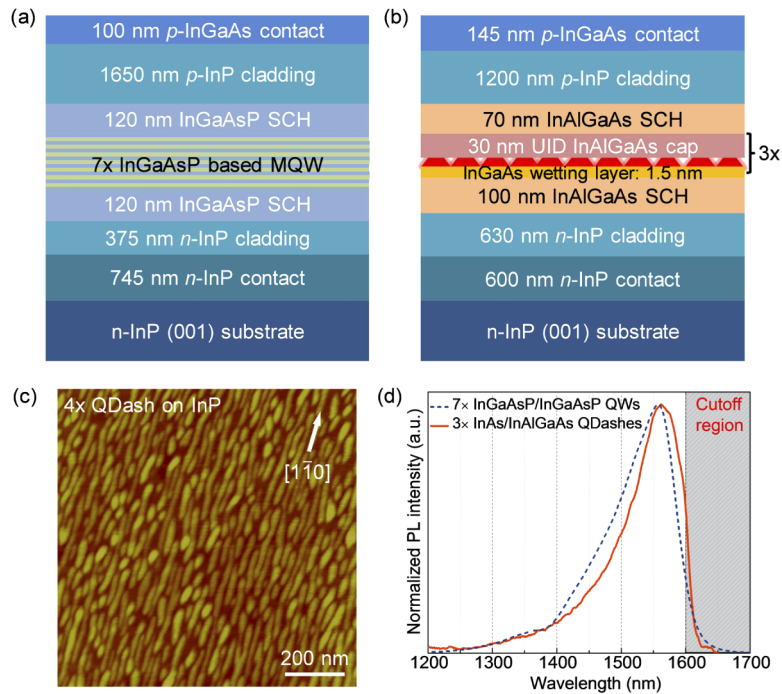


Fig. 1. MOCVD grown epi-layers for (a) seven-layer InGaAsP-based QW laser, and (b) three-stack InAs/InAlGaAs QDash laser. (c) $1 \times 1 \mu\text{m}^2$ AFM scan of the uncapped QDashes on top of three-stack InAs/InAlGaAs QDash matrix. (d) Normalized RT-PL spectra of the seven-layer QW and three-layer QDash active region, respectively.

characterized by atomic force microscope (AFM) as illustrated in Fig. 1(c). An uncapped layer of InAs QDash was grown on top of three-fold InAs/InAlGaAs matrix, elongating along the $[1\bar{1}0]$ direction. The QDash density was slightly less than $4 \times 10^{10} \text{ cm}^{-2}$. The growth details of QW and QDash laser structures have been previously reported [22,27]. The only difference is that compared to Ref. [27], here the V/III molar ratio of InAs was further reduced to 0.2 to limit the diffusion of indium adatoms, in order to form dashed structures instead of dots. The QDashes also exhibited a stronger peak intensity together with a narrower full width at half-maximum (FWHM) in photoluminescence (PL), than the QDs grown using a V/III ratio of 0.4. Normalized

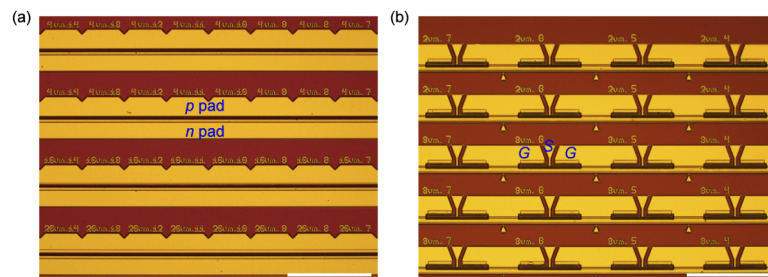


Fig. 2. Optical microscope images of fabricated devices for (a) static and (b) dynamic measurements, prior to cleavage. Metal pads and ground/signal/ground (GSG) probing are annotated in the images. The scale bars are $500 \mu\text{m}$.

room-temperature (RT) PL spectra in Fig. 1(d) demonstrate similar peak wavelengths and FWHM values for the two active material systems.

The as-grown structures were subsequently processed into surface ridge Fabry-Perot lasers. Detailed device fabrication procedures can be found in [22]. Both devices were fabricated with top side p- and n-metal contacts to facilitate high speed characterization, followed with lapping and cleavage into the same cavity dimensions. The fabricated laser bars were imaged by optical microscope in Fig. 2, for static and dynamic measurements respectively.

3. Results and discussion

3.1. Static characteristics

The thresholds for QW and QDash lasers with various cavity widths and lengths are summarized in Figs. 3(a) and 3(b). Statistically, the average J_{th} values of QW lasers are lower for all the cavity lengths and widths, due to the higher modal gains (Γg_0 , g_0 referring to the empirical gain coefficient) and lower internal losses (α_i) than the QDash ones. The lasing parameters were extracted based on the calculation methods presented in [28]. Figure 3(c) shows the inverse differential quantum efficiency ($1/\eta_d$) as a function of the cavity length for both structures. Results have suggested that the internal loss for the QDash is larger, together with a slightly larger internal quantum efficiency (η_i). The larger α_i could be ascribed to the non-optimum growth condition for QDash structures. Besides, the modal gain extrapolated in Fig. 3(d) is lower for the three-layer QDash laser primarily due to a smaller active volume and a weaker confinement factor (Γ). It was also reported that QDash laser would ideally exhibit a lower threshold in long cavities because of the reduced active material [11]. It should be emphasized that although reducing the active layer thickness could lower the threshold current density when the optical confinement is sufficiently high [29], experimentally, for a few quantum wells/dashes, the Γ and Γg_0 usually increase linearly as the active layer number increases [30]. Therefore, further optimization of QD stack number could be anticipated to increase the attainable differential gain and lower the threshold current densities. The larger differential gain also leads to a larger resonance frequency and a larger modulation bandwidth [31], and the transparent current density (J_{tr}) does not scale as the number of active layers [32]. Here the derived transparent current densities in Fig. 3(d) corresponds to 243 and 550 A/cm² per active layer for QW and QDash lasers, respectively.

Exemplary light-current-voltage (LIV) curves for $4 \times 750 \mu\text{m}^2$ devices are plotted in Fig. 3(e), indicating a larger series resistance (R_s) and a lower slope efficiency for QDash lasers. The increased R_s is ascribed to a lower doping level for n-InP cladding layer in QDash laser. The kinks in the L-I curves are related with changes in the optical mode (longitude mode hopping, mode transition, or appearance of higher order modes) in the multimode lasing spectra at progressively increased current levels. Figure 3(f) presents their lasing spectra right above the thresholds. The primary lasing peaks were both centered around 1565 nm. However, a more significant red-shift of the lasing peak was observed for QDash laser (not shown here) under continuous-wave (CW) operation, possibly due to a more severe device heating for QDashes.

To further study the thermal properties of the devices, temperature-dependent LI characteristics were measured as shown in Figs. 4(a) and 4(b). A higher maximum CW operation temperature of 90°C was achieved for QDash laser with a cavity length of 1600 μm . The corresponding T_0 values were extracted in Fig. 4(c); 78 K between 15°C and 55°C, and 48 K between 55°C and 85°C. Modulation *p*-doping of the InAs/InP QDs or QDashes have been experimentally proven effective in remarkably increasing T_0 . Besides, we also compared the thermal impedance between the two devices with a dimension of $20 \times 500 \mu\text{m}^2$:

$$Z_T = \frac{\Delta\lambda/\Delta P}{\Delta\lambda/\Delta T}. \quad (1)$$

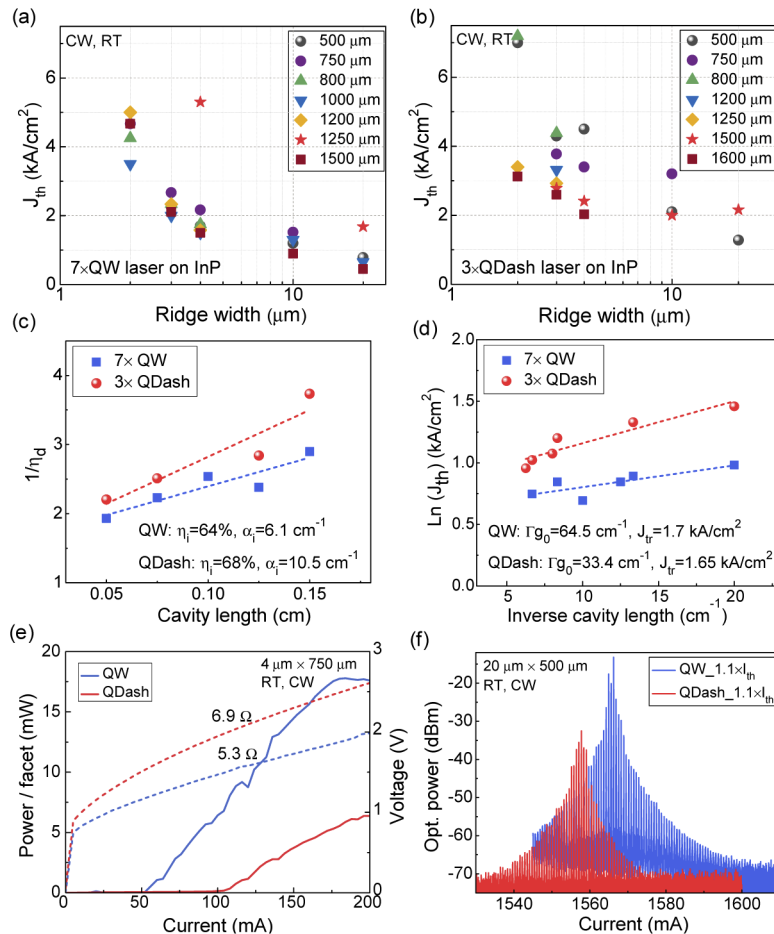


Fig. 3. Statistical threshold current density as a function of ridge width for (a) QW and (b) QDash lasers, at different cavity lengths. The inset of (a) shows the threshold current density versus inverse cavity length for both QW and QDash lasers, with a ridge width of 3 μm . (c) Dependence of inverse differential quantum efficiency ($1/\eta_d$) on cavity length, and (d) logarithm of threshold current density versus inverse cavity length for seven-layer QW and three-stack QDash lasers with a ridge width of 3 μm . (e) Exemplary LIV plots of $4 \times 750\text{ }\mu\text{m}^2$ QW and QDash lasers. (f) Lasing spectra for $20 \times 500\text{ }\mu\text{m}^2$ QW and QDash lasers with injection currents of around $1.1 \times I_{th}$.

The wavelength shift of the FP mode as a function of RT electrically dissipated power was measured under CW pumping as shown in Fig. 5(a), and the stage temperature induced wavelength shift was obtained in pulsed operation mode (300 ns pulse width, 1% duty cycle) to avoid device heating due to parasitic resistance [33]. Results have shown that the thermal impedance is slightly higher for QDashes ($Z_T = 7.3 \text{ }^\circ\text{C/W}$) than the QW laser ($5.7 \text{ }^\circ\text{C/W}$). This can be explained by the lower n-cladding doping level, thicker n-cladding layer, and the resulting larger series resistance for the QDash laser structure. Nonetheless, less wavelength temperature dependence was observed for the QDashes in pulsed operation (Fig. 5(b)), which could be attributed to the combined effects of a stronger carrier confinement and a larger conduction band-offset in the InAs/InAlGaAs material system.

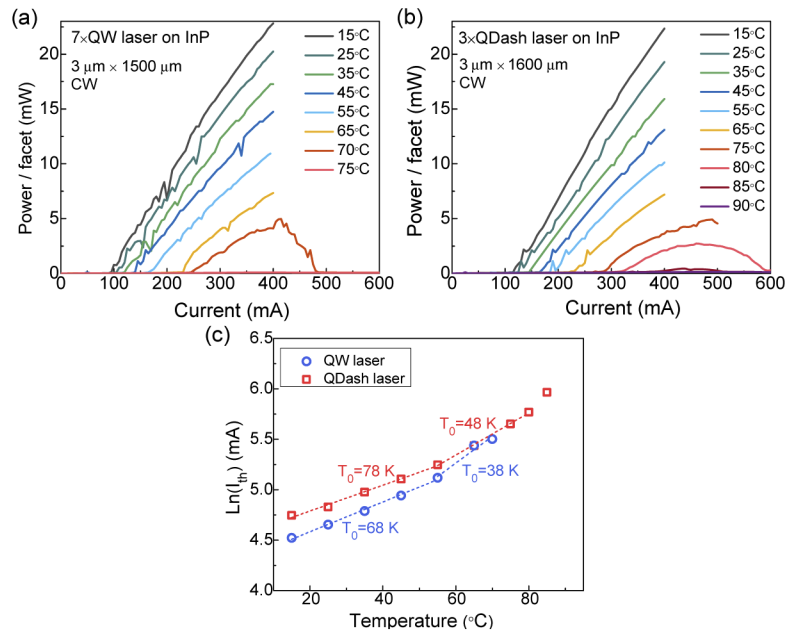


Fig. 4. Temperature-dependent L-I characteristics of (a) three-layer QDash laser, and (b) seven-layer QW laser, with similar cavity dimensions. (c) Extracted T_0 for both lasers.

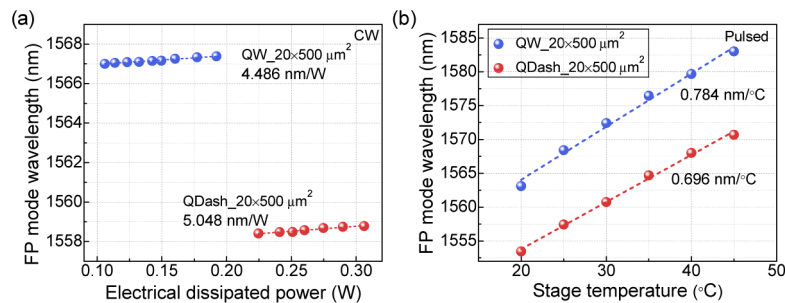


Fig. 5. FP mode wavelength shift as a function of (a) dissipated electrical power under CW excitation, and (b) stage temperature under pulsed measurement.

Figure 6 presents the dark current (I_D) investigation for $4 \times 550 \mu\text{m}^2$ QW and QDash lasers. Surprisingly, the QDashes exhibited 2-3 orders lower dark currents than the QWs at RT. As shown in Fig. 6(a), under a reverse bias of -1 V, the average dark current densities for QDash and

QW lasers were approximately $45 \mu\text{A}/\text{cm}^2$ and $45 \text{mA}/\text{cm}^2$, respectively. Here, the dark current for the QW laser is relatively high compared with the reported values in photodiodes [34], mainly due to the surface leakage induced by imperfect dry etching and sidewall passivation. Improved fabrication is expected to improve the dark current performance. Temperature-dependent dark current measurements are summarized in Fig. 6(b), from which the activation energies (ΔE_a) can be extracted. The QW curves are more convergent, indicating a weaker carrier confinement and a more severe surface leakage. The activation energy can be derived based on the Arrhenius plot shown in Fig. 6(c) [35]:

$$I_D = 2e\mu FA \left(1 + \left(\frac{\mu F}{v_s}\right)^2\right)^{-1/2} \left(\frac{m_b k T}{2\pi\hbar^2}\right)^{3/2} e^{-\Delta E_a/kT}, \quad (2)$$

where e is the electron charge, μ is the electron mobility, F is the applied electric field, A is the detection area, v_s refers to the saturation velocity of electrons, m_b is the electron effective mass in the wells/barriers, k is Boltzmann constant, and \hbar is the Planck constant. The derived ΔE_a values correlating with the electron capture potential, are 0.21 eV and 0.36 eV for QW and QDash lasers, which are approximately 26% and 45% of the RT QW and QDash bandgaps, respectively. The larger ΔE_a value for QDash structures primarily accounts for the lower dark current. As a result, the electron escape by thermionic excitation is less severe for QDash lasers, where less surface leakage could be achieved. Furthermore, the quasi-3D confinement of electrons and the larger conduction band offset for InAs/InAlGaAs QDash active region also guarantee a less sensitivity to surface leakages, resulting in lower dark currents at room temperature. Additionally, the effective mass of electrons in the two active regions were calculated to be: In_{0.73}Ga_{0.27}As_{0.85}P_{0.15} well (0.044 m_0)/In_{0.73}Ga_{0.27}As_{0.52}P_{0.48} barrier (0.064 m_0), and InAs dash (0.027 m_0)/In_{0.52}Al_{0.25}Ga_{0.23}As spacer (0.069 m_0) based on [36]. Here, m_0 represents the electron rest mass of 9.11×10^{-31} kg. The overall slightly larger electron effective mass inside the QDash active region could possibly enlarge the dark current of QDash diodes to some extent. Therefore, the thickness and composition of InAlGaAs spacer can be tuned to reduce the electron effective mass, further lowering the dark current. Note that there is always a trade-off between the dark current and responsivity [37].

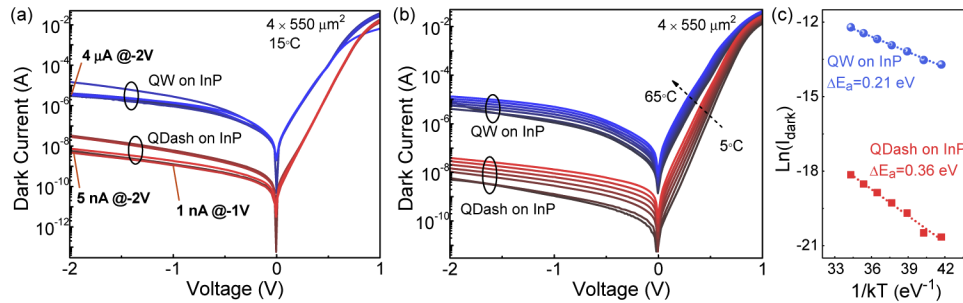


Fig. 6. (a) Statistical dark current measurements, and (b) temperature-dependent dark current evolution for QW and QDash laser on InP. (c) Arrhenius plot of the logarithm of the dark current versus the inverse temperature.

3.2. Impact of high reflection coating

To improve the device performance that could possibly suffer from a non-ideal facet cleavage, some RWG lasers with a cavity length of $550 \mu\text{m}$ were subjected to high reflectance (HR) dielectric coatings on their rear facets. The high reflectivity of 98% covers a wavelength range of $1570 \pm 20 \text{nm}$. Statistical LIV curves prior to (as-cleaved, CL) and after one facet HR coatings

are plotted in Fig. 7. Lasing parameters were further extracted in Tab. 1. In addition to enhanced performances for all the devices after HR coating, the improvement on QDashes are more arresting compared to QWs. That includes half of the average J_{th} , tripled maximum output powers, and larger slope efficiencies. The dramatic increase of output power together with reduced thresholds have also been observed for 1.3 μm HR-coated InAs/GaAs QD lasers [1,38]. Following HR coating, the lasing characteristics of QDash lasers compare favorably with the QW ones, owing to the reduced cavity loss (α_m) and threshold modal gain ($\Gamma_{g_{th}}$) [39], as well as additional facet passivation with minimized surface recombination.

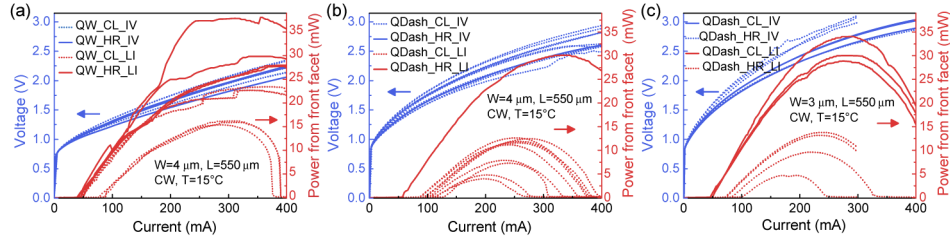


Fig. 7. Statistical LIV curves prior to and after HR coating for (a) QW and (b) QDash lasers with a cavity width of 4 μm , and (c) 3 \times 550 μm^2 QDash lasers.

Table 1. Performance comparisons between QW and QDash lasers before and after HR coatings (averaged per facet for maximum output power and slope efficiency).

Laser diodes	Device dimension	Average threshold (mA)	Average J_{th} (kA/cm^2)	Maximum output (mW)	Slope efficiency (W/A)
QW-before HR	4 \times 550 μm^2	60	2.73	19	0.18
QW-after HR	4 \times 550 μm^2	42	1.91	31	0.22
Qdash-before HR	4 \times 550 μm^2	102	4.63	9.4	0.12
Qdash-after HR	4 \times 550 μm^2	56	2.55	30	0.21
Qdash-before HR	3 \times 550 μm^2	82	4.97	10.6	0.12
Qdash-after HR	3 \times 550 μm^2	47	2.85	31	0.22

Similarly, the employment of the HR coating generates more significantly enlarged T_0 values for the QDash lasers. The effect of HR coating on the thermal properties of both QW and QDash lasers under pulsed operation is illustrated in Figs. 8(a)–8(d). Besides the increased slope efficiency, the thresholds in the high temperature regime were reduced by more than two times for QDashes, resulting in a less threshold temperature dependence. The T_0 values were further extracted in Figs. 8(e) and 8(f), under both CW and pulsed electrical injections. In contrast to the barely changed T_0 values for QW devices, the T_0 of QDash lasers increased from 54 K to 75 K between 15°C and 85°C in Fig. 8(f). The maximum operation temperature was also elevated in both operation modes, verifying a superior impact of HR coatings on improving the thermal properties of QDash or QD lasers [40].

3.3. Dynamic properties

Small signal modulation responses were measured with a vector network analyzer (VNA) to evaluate the 3-dB bandwidth (f_{3dB}) and damping. The devices were probed using a GSG probe. Figures 9(a) and 9(b) compare the normalized frequency response, S_{21} parameter, of 4 \times 550 μm^2 QW and QDash lasers at increased bias current levels. Note that these measurements were performed on devices without HR coatings. The thresholds of QW and QDash lasers extracted from LI curves were 48 mA and 86 mA correspondingly. The measured maximum f_{3dB} were accordingly 5.7 GHz and 5.5 GHz for QW and QDash lasers. The damping factor γ and relaxation

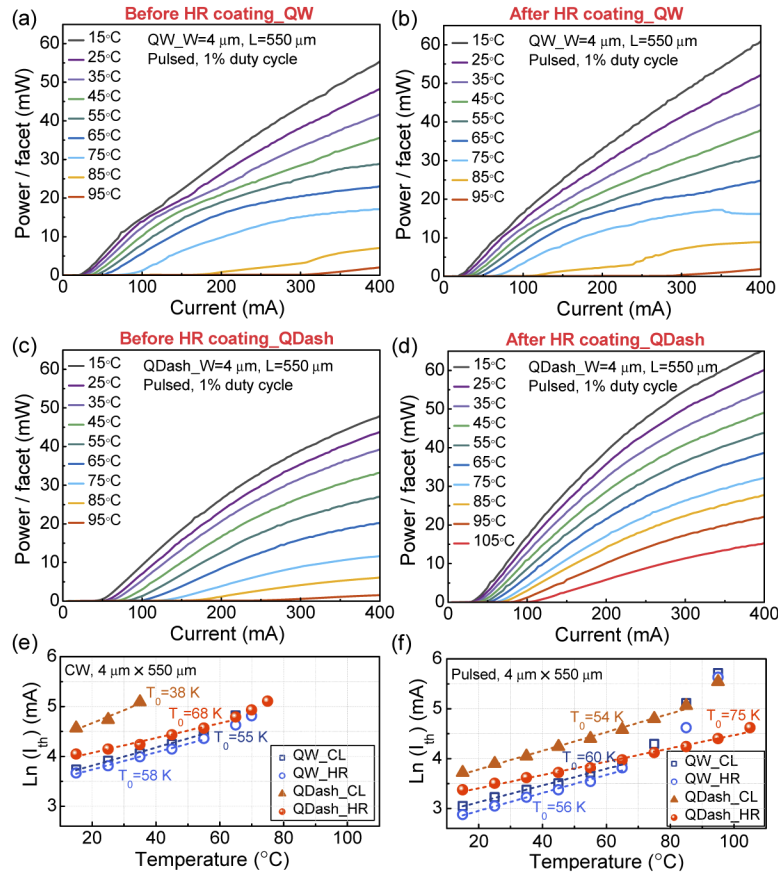


Fig. 8. Temperature-dependent L-I curves for (a,c) as-cleaved $4 \times 550 \mu\text{m}^2$ QW and QDash lasers, and (b,d) after HR coating. Extracted T_0 under (e) CW and (f) pulsed current injections.

oscillation (RO) frequency (f_r) can be acquired by fitting the formula described in Ref. [41]:

$$\text{Amplitude (f)} = 10\log_{10}\left(\frac{f_r^4}{(f^2 - f_r^2)^2 + (\gamma/2\pi)^2 f^2}\right). \quad (3)$$

It is observed from Figs. 9(a) and 9(b) that the γ value is larger for QDash laser, suggesting a stronger damping of the RO peak. The larger damping factor could be attributed to two factors: (1) the reduction of differential gain due to a lower modal gain with less active layer number [42], and some non-linear processes such as spatial hole burning and carrier heating caused by the higher carrier density in each active layer [43]; (2) the larger gain compression resulting from the lower density of lasing states compared to QW lasers. Dependence of γ on the square of f_r is shown in Fig. 9(c), which can be linearly fitted to extract the K-factor and damping offset (γ_0) [44]. The K-factor delineates the damping of the response, based on which the intrinsic modulation bandwidth (or K-factor limited maximum $f_{3\text{dB}}$) was further calculated to be 11.7 GHz and 15.7 GHz for QW and QDash lasers, respectively. Meanwhile, the carrier lifetime (τ) in the laser cavity can be quantified as $1/\gamma_0$ [25]. Therefore, the remarkably larger γ_0 of 9.52 GHz for the QDash laser corresponds to a much shorter carrier lifetime ($\tau \approx 0.11$ ns) than the QW laser ($\tau \approx 1.37$ ns). These results thus demonstrate the potential of QDash active materials for

high speed photonic device applications. Furthermore, the modulation efficiency (D^* -factor), defined as the slope of the relaxation oscillation frequency against square root of the bias current above threshold ($f_r/(I-I_{th})^{1/2}$), is fitted as 0.48 GHz/ $\sqrt{\text{mA}}$ for the QDash laser in Fig. 9(d), larger than the QW laser (0.34 GHz/ $\sqrt{\text{mA}}$). The f_r and D^* -factor can be calculated by [45]:

$$f_r = D\sqrt{P_{out}} = D^* \sqrt{I - I_{th}} = \frac{1}{2\pi} \sqrt{\frac{g_{diff} \Gamma \eta_i v_g}{e V_a}} \sqrt{I - I_{th}}, \quad (4)$$

where g_{diff} stands for the differential gain, v_g is the group velocity, and V_a is the active region volume. The D -factor here refers to the intrinsic modulation response ($D = f_r/P_{out}^{1/2}$). In our structures, the QW layer number and well thicknesses are both larger than the QDash laser, although the total active layer thicknesses are similar for both structures. Therefore, the dominant factor that leads to a higher D^* -factor for QDash laser is the lower active region volume. The D^* -factor for QDash lasers can be further improved by increasing the optical confinement and the differential gain. An earlier saturation of f_{3dB} for the QDash laser at progressively increased bias currents was also observed in the inset of Fig. 9(d), resulting from the lower differential gain and larger gain compression [25].

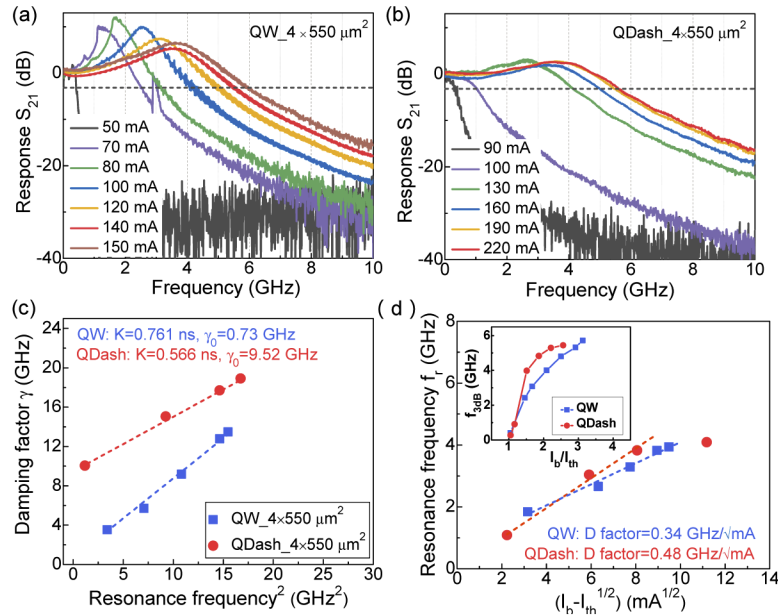


Fig. 9. (a) Small-signal frequency response measurement for $4 \times 550 \mu\text{m}^2$ QW and (b) QDash lasers at progressively increased current levels. (c) Extracted damping rate as a function of squared relaxation oscillation frequency. (d) Resonance frequency versus the root of bias currents. The inset shows the dependence of 3-dB bandwidth on the ratio of bias currents over thresholds.

The same measurements were then performed on QDash lasers with different ridge widths. The extracted K-factor, damping offset and modulation efficiency are shown in Fig. 10. Generally, a narrower ridge laser brings about higher speed modulation, and the measured maximum f_{3dB} is 7.4 GHz. The larger K-factor in narrower FP ridges is due to the increased scattering loss and more significant surface recombinations in the narrower ridges. The larger cavity loss α_m therefore results in a shorter photon lifetime (τ_p) and a lower K-factor, based on the quantitative

expressions [43]:

$$\alpha_i + \alpha_m = 1/v_g \tau_p, \quad (5)$$

$$K = 4\pi^2 \left(\tau_p + \frac{\varepsilon}{g_{\text{diff}}} \right), \quad (6)$$

where ε is the gain compression factor. These parameters are comparable with values in literature reports [11,25]. The maximum K-factor limited bandwidth is calculated as large as 32 GHz for the $3 \times 550 \mu\text{m}^2$ QDash device.

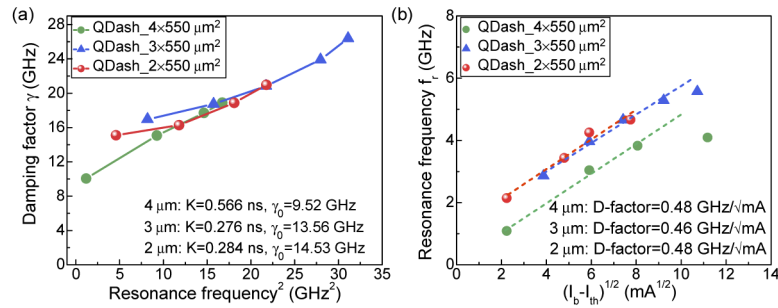


Fig. 10. (a) Dependence of damping rate on squared relaxation oscillation frequency, for QDash lasers with different ridge widths. (b) Resonance frequency as a function of the root of bias currents.

4. Conclusions

In conclusion, we have compared both static and dynamic properties of 1550 nm QW and QDash lasers grown on (001) InP substrates by MOCVD. The long cavity QDash devices exhibited a higher operation temperature and a lower threshold temperature dependence. The slightly higher thermal impedance for the QDash laser is attributed to its higher series resistance. For future optimization, the n-cladding doping level should be increased and the thickness can be cut down. It is interesting to note the remarkably reduced dark current levels by using the QDash active material. An improved dry-etching and sidewall passivation of the ridge laser would further minimize dark current, allowing the adoption of QDashes in high performance photodiodes. As to the dynamic characteristics, small signal modulation yields a larger damping factor and a higher modulation efficiency for QDash lasers. The measured 3-dB bandwidth can be as large as 7.4 GHz, and the K-factor limited bandwidth is maximized at 32 GHz for $3 \times 550 \mu\text{m}^2$ QDash lasers. The dynamic properties of the QDash laser can be further improved by optimizing the stack number to enlarge their differential gain. Moreover, the impact of HR coating on one facet was investigated on both devices and results have demonstrated a more dramatic improvement for the QDash lasers. The lasing parameters were comparable with their QW counterparts following HR coating with a reflectivity of 98% at the peak wavelength. In all, these results provide insight into C-band low dimensional quantum structures for diverse photonic device applications.

Funding

Defense Advanced Research Projects Agency (D18AP00072).

Acknowledgment

The authors acknowledge the UCSB Nanofabrication Facility staff for fabrication assistance and Dr. Gordon Keeler for technical discussions.

Disclosures

The authors declare no conflicts of interest.

References

1. G. Park, O. B. Shchekin, S. Csutak, D. L. Huffaker, and D. G. Deppe, "Room-temperature continuous-wave operation of a single-layered 1.3 μm quantum dot laser," *Appl. Phys. Lett.* **75**(21), 3267–3269 (1999).
2. D. Bimberg, M. Grundmann, and N. N. Ledentsov, "Quantum dot heterostructures," John Wiley & Sons (1999).
3. R. Schwerberger, D. Gold, J. P. Reithmaier, and A. Forchel, "Long-wavelength InP-based quantum-dash lasers," *IEEE Photonics Technol. Lett.* **14**(6), 735–737 (2002).
4. P. Bhattacharya and Z. Mi, "Quantum-dot optoelectronic devices," *Proc. IEEE* **95**(9), 1723–1740 (2007).
5. A. Y. Liu, S. Srinivasan, J. Norman, A. C. Gossard, and J. E. Bowers, "Quantum dot lasers for silicon photonics," *Photonics Res.* **3**(5), B1–B9 (2015).
6. S. Chen, W. Li, J. Wu, Q. Jiang, M. Tang, S. Shutts, S. N. Elliott, A. Sobiesierski, A. J. Seeds, I. Ross, P. M. Smowton, and H. Liu, "Electrically pumped continuous-wave III–V quantum dot lasers on silicon," *Nat. Photonics* **10**(5), 307–311 (2016).
7. K. Nishi, K. Takemasa, M. Sugawara, and Y. Arakawa, "Development of quantum dot lasers for data-com and silicon photonics applications," *IEEE J. Sel. Top. Quantum Electron.* **23**(6), 1–7 (2017).
8. L. Wang, H. Zhao, B. Shi, S. Pinna, S. T. Suran Brunelii, F. Sang, B. Song, and J. Klamkin, "High performance 1.3 μm aluminum-free quantum dot lasers grown by MOCVD," in *IEEE Opt. Fiber Comm. Conf. Exhibition (OFC)*, 1–3 (2020).
9. B. Shi, S. Zhu, Q. Li, Y. Wan, E. L. Hu, and K. M. Lau, "Continuous-wave optically pumped 1.55 μm InAs/InAlGaAs quantum dot microdisk lasers epitaxially grown on silicon," *ACS Photonics* **4**(2), 204–210 (2017).
10. N. N. Ledentsov, A. R. Kovsh, A. E. Zhukov, N. A. Maleev, S. S. Mikhlin, A. P. Vasil'ev, E. S. Semenova, M. V. Maximov, Y. M. Shernyakov, N. V. Kryzhanovskaya, V. M. Ustinov, and D. Bimberg, "High performance quantum dot lasers on GaAs substrates operating in 1.5 μm range," *Electron. Lett.* **39**(15), 1126–1128 (2003).
11. J. P. Reithmaier, A. Somers, S. Deubert, R. Schwerberger, W. Kaiser, A. Forchel, M. Calligaro, P. Resneau, O. Parillaud, S. Bansropun, M. Krakowski, R. Alizon, D. Hadass, A. Bilenca, H. Dery, V. Mikhelashvili, G. Eisenstein, M. Gioannini, I. Montrosset, T. W. Berg, M. van der Poel, J. Mørk, and B. Tromborg, "InP based lasers and optical amplifiers with wire-/dot-like active regions," *J. Phys. D: Appl. Phys.* **38**(13), 2088–2102 (2005).
12. M. Z. M. Khan, T. K. Ng, and B. S. Ooi, "Self-assembled InAs/InP quantum dots and quantum dashes: Material structures and devices," *Prog. Quantum Electron.* **38**(6), 237–313 (2014).
13. P. J. Poole, K. Kaminska, P. Barrios, Z. Lu, and J. Liu, "Growth of InAs/InP-based quantum dots for 1.55 μm laser applications," *J. Cryst. Growth* **311**(6), 1482–1486 (2009).
14. M. Borgstrom, M. P. Pires, T. Bryllert, S. Landi, W. Seifert, and P. L. Souza, "InAs quantum dots grown on InAlGaAs lattice matched to InP," *J. Cryst. Growth* **252**(4), 481–485 (2003).
15. B. Shi and K. M. Lau, "Enhanced optical properties of InAs/InAlGaAs/InP quantum dots grown by metal-organic chemical vapor deposition using a double-cap technique," *J. Cryst. Growth* **433**, 19–23 (2016).
16. A. Matsumoto, K. Akahane, T. Umezawa, and N. Yamamoto, "Extremely stable temperature characteristics of 1550-nm band, p-doped, highly stacked quantum-dot laser diodes," *Jpn. J. Appl. Phys.* **56**(4S), 04CH07 (2017).
17. K. Akahane, T. Umezawa, A. Matsumoto, N. Yamamoto, and T. Kawanishi, "Characteristics of highly stacked InAs quantum-dot laser grown on vicinal (001) InP substrate," *Jpn. J. Appl. Phys.* **55**(4S), 04EJ16 (2016).
18. M. Gendry, C. Monat, J. Brault, P. Regreny, G. Hollinger, B. Salem, G. Guillot, T. Benyattou, C. Bru-Chevallier, G. Bremond, and O. Marty, "From large to low height dispersion for self-organized InAs quantum sticks emitting at 1.55 μm on InP (001)," *J. Appl. Phys.* **95**(9), 4761–4766 (2004).
19. F. Lelarge, B. Dagens, J. Renaudier, R. Brenot, A. Accard, F. van Dijk, D. Make, O. Le Gouezigou, J. G. Provost, F. Poingt, J. Landreau, O. Drisse, E. Derouin, B. Rousseau, F. Pommereau, and G. Duan, "Recent advances on InAs/InP quantum dash based semiconductor lasers and optical amplifiers operating at 1.55 μm ," *IEEE J. Sel. Top. Quantum Electron.* **13**(1), 111–124 (2007).
20. J. P. Reithmaier, G. Eisenstein, and A. Forchel, "InAs/InP quantum-dash lasers and amplifiers," *Proc. IEEE* **95**(9), 1779–1790 (2007).
21. B. Shi, S. Zhu, Q. Li, C. W. Tang, Y. Wan, E. L. Hu, and K. M. Lau, "1.55 μm room-temperature lasing from subwavelength quantum-dot microdisks directly grown on (001) Si," *Appl. Phys. Lett.* **110**(12), 121109 (2017).
22. B. Shi, H. Zhao, L. Wang, B. Song, S. T. Suran Brunelli, and J. Klamkin, "Continuous-wave electrically pumped 1550 nm lasers epitaxially grown on on-axis (001) silicon," *Optica* **6**(12), 1507–1514 (2019).
23. I. Alghorabi, L. Joulaud, C. Paranthoen, A. Le Corre, O. Dehaese, N. Bertru, H. Follot, P. Caroff, and S. Loualiche, "InAs self-assembled quantum dot and quantum dash lasers on InP for 1.55 μm optical telecommunications," in *2nd IEEE Inter. Conf. Info. Comm. Technol. (ICICT)* 2, 2085–2090 (2006).
24. A. J. Zilkie, J. Meier, M. Mojahedi, P. J. Poole, P. Barrios, D. Poitras, T. J. Rotter, C. Yang, A. Stintz, K. J. Malloy, P. W. E. Smith, and J. S. Aitchison, "Carrier dynamics of quantum-dot, quantum-dash, and quantum-well semiconductor optical amplifiers operating at 1.55 μm ," *IEEE J. Quantum Electron.* **43**(11), 982–991 (2007).
25. T. Sadeev, D. Arsenijević, and D. Bimberg, "Comparison of dynamic properties of InP/InAs quantum-dot and quantum-dash lasers," *Appl. Phys. Lett.* **109**(16), 161104 (2016).

26. B. Shi and J. Klamkin, "Defect engineering for high quality InP epitaxially grown on on-axis (001) Si," *J. Appl. Phys.* **127**(3), 033102 (2020).
27. S. Zhu, B. Shi, Q. Li, and K. M. Lau, "1.5 μm quantum-dot diode lasers directly grown on CMOS-standard (001) silicon," *Appl. Phys. Lett.* **113**(22), 221103 (2018).
28. S. Zhu, B. Shi, Q. Li, and K. M. Lau, "Room-temperature electrically-pumped 1.5 μm InGaAs/InAlGaAs laser monolithically grown on on-axis (001) Si," *Opt. Express* **26**(11), 14514–14523 (2018).
29. M. Rosenzweig, M. Mohrle, H. Duser, and H. Venghaus, "Threshold-current analysis of InGaAs-InGaAsP multi-quantum well separate-confinement lasers," *IEEE J. Quantum Electron.* **27**(6), 1804–1811 (1991).
30. G. Hunziker, W. Knop, and C. Harder, "Gain measurements on one, two, and three strained GaInP quantum well laser diodes," *IEEE J. Quantum Electron.* **30**(10), 2235–2238 (1994).
31. Y. Arakawa and A. Yariv, "Quantum well lasers—Gain, spectra, dynamics," *IEEE J. Quantum Electron.* **22**(9), 1887–1899 (1986).
32. B. Zhao, T. R. Chen, and A. Yariv, "The extra differential gain enhancement in multiple-quantum-well lasers," *IEEE Photonics Technol. Lett.* **4**(2), 124–126 (1992).
33. B. Shi, S. Pinna, B. Song, H. Zhao, and J. Klamkin, "Thermal impedance and gain switching of 1550 nm room temperature continuous-wave electrically pumped laser diode monolithically grown on silicon," in *IEEE Opt. Fiber Comm. Conf. Exhibition (OFC)* 1–3 (2020).
34. J. F. Klem, J. K. Kim, M. J. Cich, G. A. Keeler, S. D. Hawkins, and T. R. Fortune, "Mesa-isolated InGaAs photodetectors with low dark current," *Appl. Phys. Lett.* **95**(3), 031112 (2009).
35. H. Bai, J. Zhang, X. Wang, and X. Liu, "Characteristics analysis of dark current in quantum dot infrared photodetectors," *Opt. Laser Technol.* **48**, 337–342 (2013).
36. E. H. Li, "Material parameters of InGaAsP and InAlGaAs systems for use in quantum well structures at low and room temperatures," *Phys. E* **5**(4), 215–273 (2000).
37. Y. W. Chen, W. C. Hsu, R. T. Hsu, Y. H. Wu, and Y. J. Chen, "Low dark current InGaAs (P)/InP p–i–n photodiodes," *Jpn. J. Appl. Phys.* **42**(Part 1, No. 7A), 4249–4252 (2003).
38. H. Y. Liu, D. T. Childs, T. J. Badcock, K. M. Groom, I. R. Sellers, M. Hopkinson, R. A. Hogg, D. J. Robbins, D. J. Mowbray, and M. S. Skolnick, "High-performance three-layer 1.3- μm InAs-GaAs quantum-dot lasers with very low continuous-wave room-temperature threshold currents," *IEEE Photonics Technol. Lett.* **17**(6), 1139–1141 (2005).
39. S. J. Jang, C. I. Yeo, J. S. Yu, and Y. T. Lee, "Performance improvement by metal–dielectric HR coating in laterally coupled DFB laser with metal surface gratings," *Appl. Phys. B* **100**(3), 553–558 (2010).
40. I. R. Sellers, H. Y. Liu, K. M. Groom, D. T. Childs, D. Robbins, T. J. Badcock, M. Hopkinson, D. J. Mowbray, and M. S. Skolnick, "1.3 μm InAs/GaAs multilayer quantum-dot laser with extremely low room-temperature threshold current density," *Electron. Lett.* **40**(22), 1412–1413 (2004).
41. P. A. Morton, T. Tanbun-Ek, R. A. Logan, A. M. Sergent, P. F. Sciortino, and D. L. Coblenz, "Frequency response subtraction for simple measurement of intrinsic laser dynamic properties," *IEEE Photonics Technol. Lett.* **4**(2), 133–136 (1992).
42. M. C. Tatham, I. F. Lealman, C. P. Seltzer, L. D. Westbrook, and D. M. Cooper, "Resonance frequency, damping, and differential gain in 1.5 μm multiple quantum-well lasers," *IEEE J. Quantum Electron.* **28**(2), 408–414 (1992).
43. T. Fukushima, R. Nagarajan, M. Ishikawa, and J. E. Bowers, "High-speed dynamics in InP based multiple quantum well lasers," *Jpn. J. Appl. Phys.* **32**(Part 1, No. 1A), 70–83 (1993).
44. L. A. Coldren, S. W. Corzine, and M. L. Mashanovitch, "Diode lasers and photonic integrated circuits," John Wiley & Sons 218, (2012).
45. D. Tauber, G. Wang, R. S. Geels, J. E. Bowers, and L. A. Coldren, "Large and small signal dynamics of vertical cavity surface emitting lasers," *Appl. Phys. Lett.* **62**(4), 325–327 (1993).